





## Article

# Spatial Mapping of Groundwater Potentiality Applying Geometric Average and Fractal Models: A Sustainable Approach

Fatima Zahra Echogdali <sup>1</sup>, Said Boutaleb <sup>1</sup>, Mohamed Abioui <sup>1,2,\*</sup> , Mohamed Aadraoui <sup>3</sup>, Amine Bendarma <sup>4</sup> , Rosine Basseu Kpan <sup>5</sup>, Mustapha Ikirri <sup>1</sup>, Manal El Mekkaoui <sup>1</sup> , Sara Essoussi <sup>1</sup>, Hasna El Ayady <sup>1</sup>, Kamal Abdelrahman <sup>6</sup>  and Mohammed S. Fnais <sup>6</sup>

<sup>1</sup> Department of Earth Sciences, Faculty of Sciences, Ibn Zohr University, Agadir 80000, Morocco

<sup>2</sup> MARE—Marine and Environmental Sciences Centre-Sedimentary Geology Group, Department of Earth Sciences, Faculty of Sciences and Technology, University of Coimbra, 3030-790 Coimbra, Portugal

<sup>3</sup> Laboratory of Geo-Ressources and Environment, Faculty of Science and Technology, Sultan Moulay Slimane University, Beni Mellal 23000, Morocco

<sup>4</sup> Laboratory for Sustainable Innovation and Applied Research, Universiapolis—International University of Agadir, Agadir 80000, Morocco

<sup>5</sup> Regional Water and Environmental Sanitation Centre Kumasi, Kumasi 5028, Ghana

<sup>6</sup> Department of Geology & Geophysics, College of Science, King Saud University, Riyadh 11451, Saudi Arabia

\* Correspondence: m.abioui@uiz.ac.ma

**Abstract:** Water scarcity affects all continents, with approximately 1.2 billion people living in areas where water is physically lacking. This scarcity is more accentuated in countries with an arid climate, and its impact becomes more threatening when the economy depends mainly on it. The Kingdom of Morocco, with its agricultural vocation, is one of them, especially in its southern regions. Therefore, mapping areas with high groundwater potential based on available geospatial data allows for optimizing the choice of a future well in such areas. Geometric average and fractal models were used to assess and delineate potential groundwater areas in the Tissint basin, Southeast Morocco. Eight factors, including topography, geology, hydrology, and hydrogeology, influencing the distribution of water resources was used. The formation permeability factor presents the most significant impact among the others, although it is directly related to most of them. The areas located in the central and downstream part of the basin are characterized by a high water potentiality due to increased geological formations' permeability near the drainage system, which constitutes a recharge zone, and a low slope allowing a prolonged water-formation contact time favoring a gradual infiltration of the water towards the deep aquifers. The groundwater potential map has been edited and validated by comparing it with data from 52 wells scattered throughout the basin. The favorable potential sectors cover 15.81% of the basin's total area. The moderate ones account for 21.36% while the unfavorable areas cover 62.83%. These results aim to provide policymakers and managers with a guide map for groundwater research and reduce hydrogeological investigation costs.

**Keywords:** groundwater potential areas; geometric average model; fractal model; tissint; Morocco



**Citation:** Echogdali, F.Z.; Boutaleb, S.; Abioui, M.; Aadraoui, M.; Bendarma, A.; Kpan, R.B.; Ikirri, M.; El Mekkaoui, M.; Essoussi, S.; El Ayady, H.; et al. Spatial Mapping of Groundwater Potentiality Applying Geometric Average and Fractal Models: A Sustainable Approach. *Water* **2023**, *15*, 336. <https://doi.org/10.3390/w15020336>

Academic Editor: Alexander Yakirevich

Received: 29 October 2022

Revised: 6 January 2023

Accepted: 8 January 2023

Published: 13 January 2023



**Copyright:** © 2023 by the authors. Licensee MDPI, Basel, Switzerland. This article is an open access article distributed under the terms and conditions of the Creative Commons Attribution (CC BY) license (<https://creativecommons.org/licenses/by/4.0/>).

## 1. Introduction

Groundwater is the most extracted resource globally with withdrawal rates currently approaching 982 km<sup>3</sup>/year [1]. Approximately 70% of this exploited resource is used both for agriculture (33%) and drinking water supply (37%) [2,3]. Continued overexploitation of this precious resource threatens future generations [4,5]. As pressure on this resource continually increases, the delineation of its potential areas becomes essential for its protection and better management [6].

In arid and semi-arid regions, water demand considerably increases, leading to a water shortage that does not stop worsening due to this resource's overexploitation and

climate change's impact [7,8]. Morocco, like other arid countries in the world, is heading a water resources crisis due to its climatological conditions and the degradation of part of its resources [9]. Its topography, mountainous type in more than 75% of the surface, induces a dominance of hard rock aquifers in which the presence of groundwater depends on several climatological, topographical, geological, and hydrogeological factors [10–13]. In recent years, several studies relating to mapping the groundwater potential areas (GWPA) have been done in many arid countries, such as Morocco [14–17], Tunisia [18], Saudi Arabia [19], India [20], and Mexico [21]. They used various statistical models that successfully outperformed traditional hydrogeological prospecting approaches [22,23].

Three main models exist for mapping groundwater potential areas:

- (1) Data-Driven-Model, which concerns statistical, probabilistic, and data mining techniques and the quality and quantity of data are the significant characteristics impacting the predictive precision. Various types of the first model have been employed for editing groundwater potential area maps, such as Dempster-Shafer theory [24,25], evidential belief function [26,27], frequency ratio [28,29], logistic regression [30,31], statistical index [25], certainty factor [32,33], the weight-of-evidence method [34] and index of entropy [35];
- (2) Knowledge-based models, e.g., analytical hierarchy process (AHP), are based on expert experience [36,37] and are thus affected by the knowledge and subjectivity of experts, while they are also generally site-specific [38];
- (3) Machine learning techniques (MLTs) have provided better accuracy in many situations due to their ability to handle, in a robust manner, data characterized by a non-linear format, representing different scales, and deriving from different sources [39,40]. The MLT includes several models such as aquifer sustainability factor [41], classification and regression tree [42], random forest [22,43], boosted regression tree [44], maximum entropy [22], artificial neural network model [45], and generalized additive model [46].

This paper suggests a new method (geometric average model) for mapping groundwater potential areas in the Tissint basin (Morocco). This method has been tested in the Akka basin (Morocco) and compared with the excepted value model [17]. The GA model is a correct statistical averaging model, mainly when calculating a single average of potential groundwater based on various factors impacting the availability of this resource. It is used to (1) reduce the uncertainty associated with bias in factor weights, (2) allow for the problem of using different evidence layer values in the same unit, and (3) provide fuzzy weights of continuous values in the factor maps that are assigned [47]. The prediction-area graph (P-A) [48,49] and the normalized density and its weight [50] are used to estimate the prediction capacity of this model.

The GA model application aims to establish a reliable groundwater potential map verified by the existing wells in the Tissint basin.

## 2. Study Area

The Tissint basin, with a surface area of 3595.87 km<sup>2</sup>, is located in the southeastern region of Morocco (Figure 1). It extends between X (250,000 to 350,000) and Y (31,000 to 374,000) Lambert Coordinates with a mountainous topography where altitudes vary from 564 to 2149 m. The climate is mainly arid and characterized by low rainfall, 100 mm on average, which generally faces summer temperatures exceeding 40 °C. More than 90% of the annual rainfall occurs from September to April. The hydrographic basin network, constituted by a set of tributaries (Assif N'Tamsoult and Assif Sidi Lahcen to the north and Assif N'Tinguissint to the east), converges downstream at Tissint Fom. On the hydrogeological level, the Plio-quadernary filling of the beds of the Tissint wadi reaches several tens of meters, constituting in places alluvial aquifers captured by a set of boreholes whose maximum flow rates reach 25 L/s.

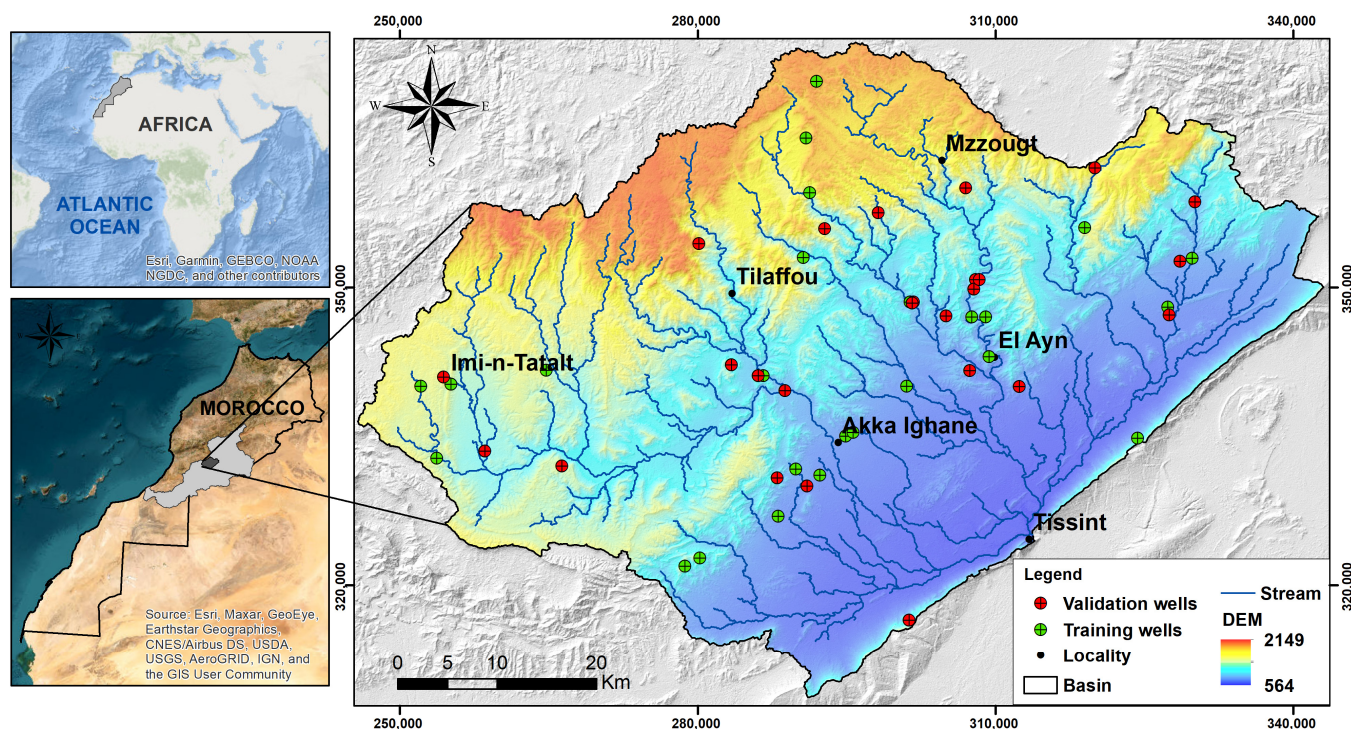


**Figure 1.** Tissent basin location with the Digital Elevation Model (DEM).

Geologically, the basin is part of the Western Anti-Atlas chain. It consists of Proterozoic formations outcropping in the inliers [51], under a Paleozoic sedimentary cover folded during the variscan events [52]. This late Neoproterozoic (Adoudounian) and Paleozoic cover begin with carbonate deposits forming the Adoudounian “lower limestones” and are overlain by pelites interspersed with carbonate beds of the “lie-de-vin series” attributed to the Lower Cambrian, followed by carbonate deposits of the “upper limestone” and the shaly limestone series [51,53–57]. The remaining Paleozoic series outcrops in the southeast of the basin where Ordovician detrital facies (sandstones) form the Jbel Bani ridge. These formations are arranged on anticlinal bulges consisting of Precambrian metamorphic and granitic formations [58,59] (Figure 2).

The Quaternary formations rest directly on Paleozoic substrates and comprise the principal groundwater aquifer in the Tissent Basin. Groundwater flow is primarily in the Quaternary formations and places by upward drainage through fractures. The hydrogeological properties of this alluvial system are highly dependent on the pre-Saharan climate and local arid conditions that make evaporation very intense in the groundwater discharge process. At the same time, the aquifer is subject to constraints that depend on the weak role of precipitation in the development of groundwater. The geological structure of the study area precludes the existence of a deep groundwater reservoir and instead facilitates the development of a groundwater resource in the Quaternary alluvial cover.



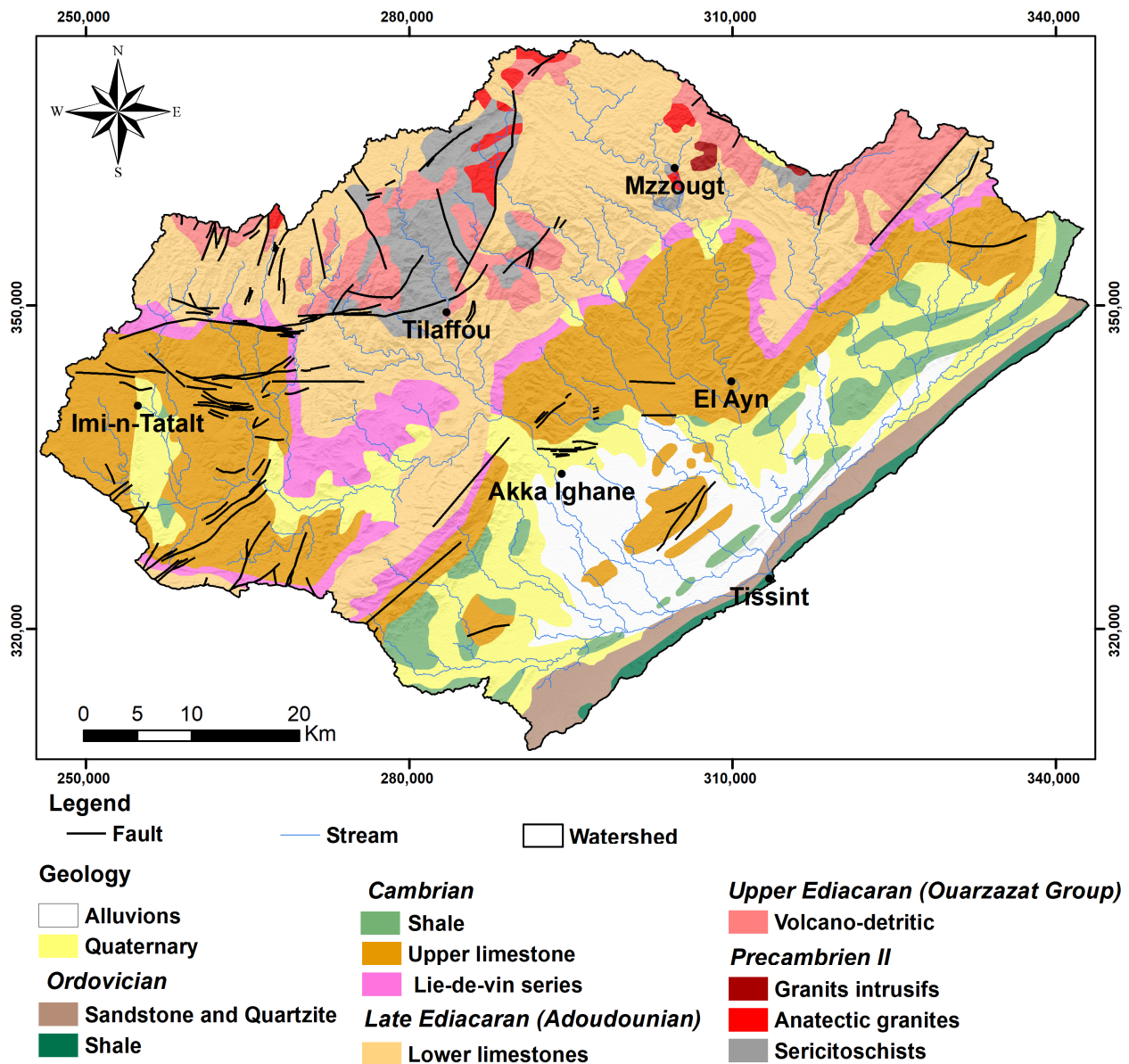


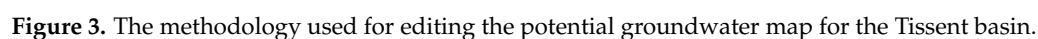
Figure 2. Geological map of Tissint basin.

### 3. Materials and Methods

The methodology used for editing the potential groundwater map is presented in Figure 3 and summarized in the following steps:

- (1) Collect the locations of wells from the Souss Massa Hydraulic Basin Agency by random distribution [12]. Divide the data set of 52 wells into two categories; use 50% (26 wells) for training, and use the rest (26 wells) for validation [60].
- (2) Collect a geospatial database that influences groundwater availability from different sources and generate different map factors.
- (3) Assign a score to the classes of each factor according to their relative importance using the logistic function.
- (4) Select effective and ineffective factors by assigning weights using Concentration-Area (C-A) and Prediction-Area (P-A).
- (5) Generate the groundwater potential map by applying the Geometric Average Model (GAM).
- (6) Validate the efficiency and predictive ability of the model using 50% of the well locations.





Different geospatial data sets (Table 1) were designed to establish a potential groundwater map based on the literature review. Eight factors impacting groundwater availability are incorporated into the GA model: lineament, node and drainage densities, river and lineament distances, permeability, elevation, and slope [11,16,17,61,62]. Although other authors use more factors, we limit ourselves to only eight with the non-existence of both climatological stations in the basin and high-resolution geospatial data. The permeability map was generated from the geological map of 1:1,000,000 scale, collected from the Moroccan Energy and Mines Ministry. The DEM (Digital Elevation Model) was downloaded from USGS (<http://earthexplorer.usgs.gov/> (accessed on 23 September 2014)) and was used to derive the slope, altitude, and river maps. The drainage density and the distance from rivers maps were produced using the Line Density and Euclidean distance, respectively, in the spatial analysis extension of ArcGIS. Lineaments were extracted from Landsat 8 OLI images acquired on 30 December 2021, and the faults were digitized from the geological

map of 1:1,000,000 scale. Finally, the lineament and the node densities were edited using the ArcGIS functions.

**Table 1.** Database of the Tissent basin.

Category	Factor	Data Type	Scale	Source
Topographical	Slope	Raster	30 m × 30 m	DEM ( <a href="http://earthexplorer.usgs.gov/">http://earthexplorer.usgs.gov/</a> (accessed on 23 September 2014))
	Altitude	Raster	30 m × 30 m	DEM ( <a href="http://earthexplorer.usgs.gov/">http://earthexplorer.usgs.gov/</a> (accessed on 23 September 2014))
Hydrological	Distance from rivers	Raster	30 m × 30 m	DEM ( <a href="http://earthexplorer.usgs.gov/">http://earthexplorer.usgs.gov/</a> (accessed on 23 September 2014))
	Drainage density	Raster	30 m × 30 m	DEM ( <a href="http://earthexplorer.usgs.gov/">http://earthexplorer.usgs.gov/</a> (accessed on 23 September 2014))
Geological	Permeability	Raster	1:1,000,000	Geological map of Morocco (Ministry of Energy and Mines of Morocco)
	Lineament density	Raster	30 m × 30 m	Landsat 8 OLI ( <a href="http://earthexplorer.usgs.gov/">http://earthexplorer.usgs.gov/</a> (accessed on 30 December 2021))
	Node density	Raster	30 m × 30 m	Landsat 8 OLI ( <a href="http://earthexplorer.usgs.gov/">http://earthexplorer.usgs.gov/</a> (accessed on 30 December 2021))
	Distance from lineament	Raster	30 m × 30 m	Landsat 8 OLI ( <a href="http://earthexplorer.usgs.gov/">http://earthexplorer.usgs.gov/</a> (accessed on 30 December 2021))
Groundwater Point	Well	Vector	-	The Souss Massa Hydraulic Basin Agency (Agadir, Morocco)

### 3.2. Methods Used

#### 3.2.1. Generation of Decision Factors with Logistic Transformation

Transformation of the values of the factors into a logistic space provides a set of values with more discriminatory information and facilitates their interpretation [63,64]. It is due to using a sigmoid logistic function that allows for obtaining an optimal decision limit for the classification [49,65]. Yousefi et al. [66] demonstrated that the sigmoid logistic function could transform individual data from different data sets in the same space. Therefore, it can assess the potential groundwater area maps. The logistic function converts unlimited values in the same logistic space range [0–1] [64,65]. A score of 1 is assigned to the “very low” or “very high” classes depending on whether they contribute to the excellent performance of the considered indicator. In the opposite case, a score of 0 is assigned to these classes. Following the same logic, intermediate values go to the middle classes according to a linear distribution. Yousefi and Carranza [67] applied the non-linear sigmoid logistic function to transform different data in the same space:

$$F_X = \frac{1}{1 + e^{-s(X-i)}} \quad (1)$$

where  $F_X$  and  $X$  are, respectively, the value transformed in the logistic space, and as the raw value of each pixel of the input factor,  $i$  and  $s$  are, respectively, the inflection point and the slope of the logistic function. Therefore, these two parameters can be computed using the following equations [48]:

$$i = \frac{2\ln 99}{\max(X) - \min(X)} \quad (2)$$

$$s = \frac{\max(X) + \min(X)}{2} \quad (3)$$

After assigning continuous fuzzy evidence scores using logistic functions, the edited factor maps are combined to obtain a groundwater potentiality area map (GWPA). Data from 26 wells are used to evaluate this GWPA map.

### 3.2.2. Identify the Best-Performing Factor

The prediction capacity of each factor used to delineate GWPA can vary for different regions. For that reason, assessing the importance of each of them is essential to consider in the prospecting model [67]. First, the location of known wells is combined on a classified factor map to determine the credibility of the factors used [66,68,69]. The Prediction-Area (P-A) graph is then applied to assess and distinguish efficient and inefficient factors. Next, the occurrence prediction rate curve of wells corresponding to the class of weighted factor layer and the percentage curve of occupied areas corresponding to the rank of weighted factor layer is executed. Finally, the intersection points in the P-A graph are extracted and applied to calculate the normalized density index ( $N_d$ ) and its weights ( $W_e$ ) [67,70].  $N_d$  is calculated as a ratio between the prediction rate and the corresponding occupied area using the following equation:

$$N_d = \frac{P_r}{O_a} \quad (4)$$

where  $N_d$  is the normalized density,  $P_r$  and  $O_a$  are the prediction rate and occupied area extracted from the P-A intersection point, respectively, and  $W_e$  are the weight calculated by considering the  $\ln$  of  $N_d$  [70]. A value of  $N_d > 1$  ( $W_e > 0$ ) for a factor map indicates a positive association that meets the criteria for delineating target areas for further exploration.

Various models, such as Concentration-Perimeter [71], Spectrum-Area [72], Concentration-Volume [73], Number-Size [74,75], and Concentration-Distance [76], have been successfully applied to deal with geoscience data and geospatial models [77,78]. In this study, the Concentration-Area (C-A) fractal model proposed by Cheng et al. [79] was used to determine the factor values discretized threshold, which subsequently allowed the editing of discretized weighted evidence maps. The most powerful features of this model are the simple implementation and the ability to calculate quantitative anomalous thresholds [79–82]. Straight-line segments determine fractal dimensions with a uniform slope in the log-log plot [83]. The line segment slope breaks and corresponding values could be used as a cut-off for factor delineation, and classification [49,50,84–86].

### 3.2.3. Integration of Transformed Factors

The integration of transformed factors has been done using multi-criteria decision-making functions [87,88], allowing targeting and determining the groundwater potential areas. The geometric average ( $G_A$ ) model combining method was used to produce a potentiality model in a GIS environment. Due to the complexity of the numbers, it is not easy for anyone other than a mathematician to understand and calculate them [89]. It cannot be calculated in the case of a negative or zero value of any variable.  $G_A$  model is defined as the  $n$ th root of the products of values where  $n$  is the count of values. The geometric average,  $G_A$  of a data set  $\{v_1, v_2, \dots, v_n\}$  is given by [47]:

$$G_A(v_1, v_2, \dots, v_n) = \left( \prod_{i=1}^n v_i \right)^{1/n} = \sqrt[n]{v_1 v_2 \dots v_n} \quad (5)$$

### 3.2.4. Model Validation

Validation of results is considered the most crucial process in modeling, without which a model is scientifically worthless [90]. The GWPA map was confirmed by correlating the potentiality classes with the spatial distribution of validation wells not used as a database in the model development [16].



## 4. Results

### 4.1. Identification of Decision Factors

#### 4.1.1. Drainage Density

Drainage density is directly related to precipitation, topography, and geomorphology [91]. It is defined as the ratio of the sum of streams to the total basin area. Determination of drainage density indicates areas of water recharge to deep aquifers. Thus, areas of high drainage density have high runoff and low infiltration rates and vice versa [62]. The drainage density map is divided into four classes: very high, high, moderate, and low representing, respectively, 15.58%, 17.02%, 22.36%, and 45.04% of the basin area. The areas of high drainage density are located in the downstream and western parts of the basin while the areas of low density occupy the rest (Figure 4a).

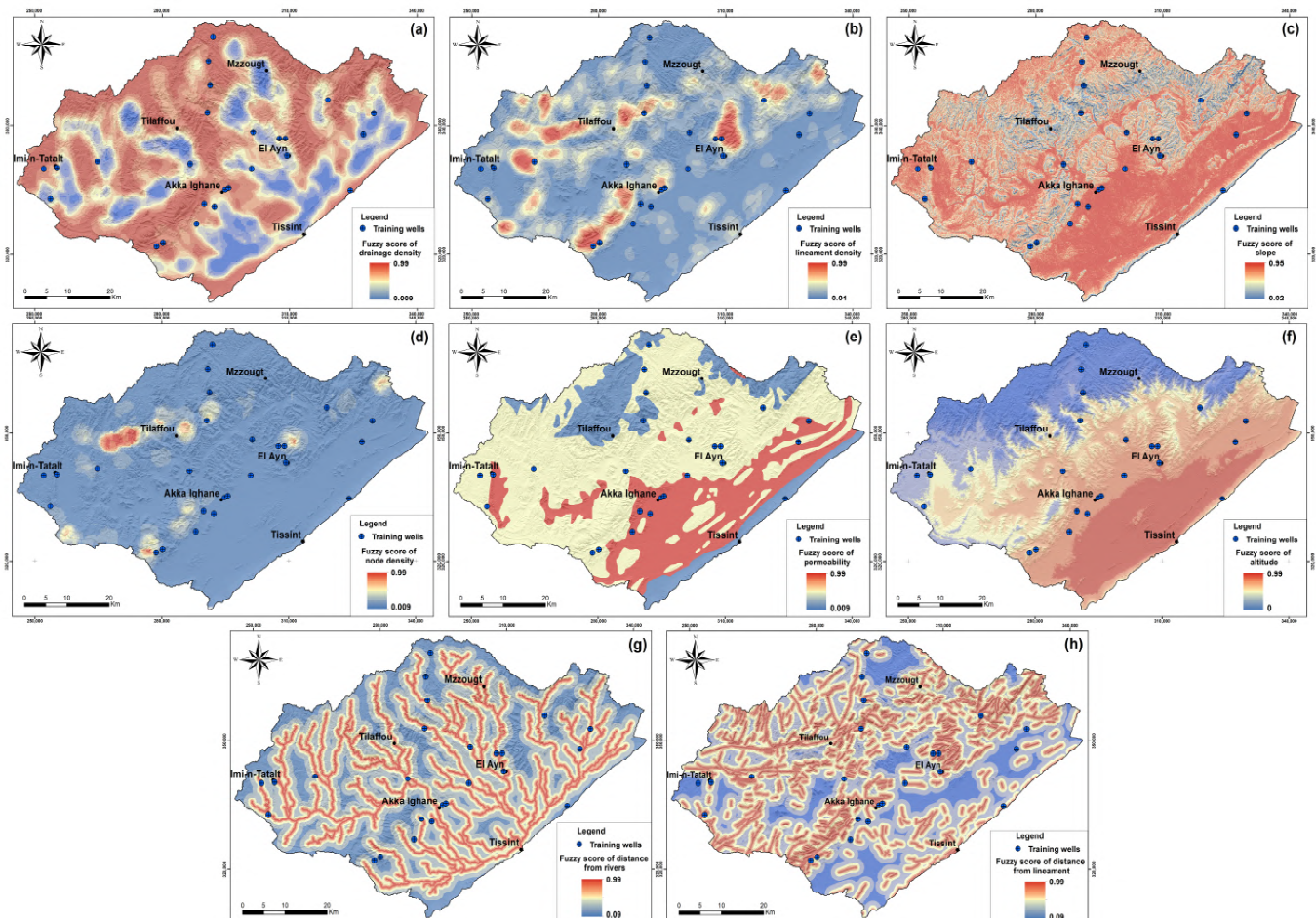


**Figure 4.** Maps of transformed values: (a) drainage density map; (b) lineament density map; (c) slope map; (d) node density map; (e) permeability map; (f) altitude map; (g) distance from rivers map; (h) distance from lineament map.

#### 4.1.2. Lineament Density

Hydrogeological lineaments are the most structural in groundwater recharge, allowing rainwater infiltration and storage [91]. They represent fractures, joints, and faults that appear as linear lines on the earth's surface in satellite images [92]. Hard-rock formations with low primary porosity characterize arid and semi-arid regions, and therefore, groundwater is generally found in faults and weathering areas concentrated along these faults [93]. Conversely, areas with a high lineament density indicate a higher infiltration rate and, therefore, a higher groundwater potential [94].

This study uses the Analysis of Principal Components (ACP) to identify and map the lineaments. Subsequently, Haris et al. [95] proposed the Sobel directional filtering technique for the four directions E-W, N-S, NW-SE, and NE-SW to extract lineaments. Non-structural lineaments, such as roads, electricity networks, and canals, are eliminated to improve the results [96–99]. The final map has been elaborated, combining lineaments from satellite images and digitalized faults from geological maps of Morocco (1:1,000,000) in the study area. Lineaments density map is divided into five categories: very high, high, moderate, low, and very low, representing 3.12%, 4.52%, 7.11%, 17.80%, and 67.45% of the total areas. Due to their direct relationship with the groundwater, a very high density of lineaments is found in the northeastern, southwestern, and western parts of the basin. On the other hand, the very low and low densities are located downstream and north of the basin (Figure 4b).

#### 4.1.3. Slope

The slope is a factor that influences rainfall retention and infiltration [100]. It represents an inverse relationship to infiltration and a proportional relationship to runoff [101]. The slope of the basin varies from 0 to 75%. Five classes were identified in the entire basin: very low (42.32%), low (26.90%), moderate (19.38%), high (8.69%), and very high (2.71%). High and very high classes represent only 11.40% of the total area while 69.22% is dominated by a low and very low slope (Figure 4c).

#### 4.1.4. Node Density

The nodes represent the intersection point of two or many lineaments [16]. Their sites are favorable for groundwater accumulation, and they are critically used in prospecting groundwater potential areas. In a SIG environment, the node map was designed from hydrogeological lineaments. A more significant part of the basin is characterized by a low node density, covering 91.62%; these areas are unfavorable for the presence of groundwater. Therefore, the lowest weight was assigned to this class. Based on Figure 4d, regions with a high node density, covering 2.90% of the area, are found in the north of the El Ayn region and the southwest of Akka Ighane village. They are identified as areas likely to develop a very high groundwater potential. As those localities are also located in high lineament density areas, the two factors are the place of interest for the development of groundwater.

#### 4.1.5. Permeability

Acharya and Nag [102] integrate the lithological factor for its direct or indirect influence on water infiltration. Surface water runoff is high in hard-rock formations and very low in loose and porous formations, where infiltration is controlled by the grain size and the rock porosity [93]. The Tissent basin mainly consists of a Paleozoic formation made up of limestone and shales with a moderate permeability within a range of [0.17–0.70], occupying 61.05% of the basin. They are followed by the quaternary formation of high permeability comprising mainly alluvial deposits within a range of [0.70–0.99] whose lithology is more favorable to surface water infiltration and that represents 22.76% of the area. Finally, the northeast part of the basin, which is characterized by shales and Precambrian gneissic and granite complexes, presents low permeability within a range of [0.009–0.17], occupying 16.19% of the total basin (Figure 4e).

#### 4.1.6. Altitude

Altitude is a factor that controls groundwater availability. Low altitudes induce surface water retention, leading to infiltration and recharge, and generate low runoff rates, whereas high runoff rates and low infiltration are associated with high altitudes [103,104]. Five classes are defined based on altitude variation: 564–863 (29.26%), 863–1125 (20.48%), 1125–1384 (19.83%), 1384–1693 (15.67%), and 1693–2149 (14.76%). The lowest ones are found on the basin's downstream part and are constituted by alluvial formations. The higher (30.43%) occupy the northern part of the basin (Figure 4f).

#### 4.1.7. Distance from Lineament

The fractured formations are likely to be weathered and present a high infiltration rate. The lineaments behave as canals for groundwater flow and are, therefore, important for infiltration [105]; the presence of water resources decreases with the distance from lineaments. Therefore, the best opportunity to target new groundwater exploitation areas is close to lineaments positions [106]. Areas near the lineaments show an excellent relationship with water availability. Therefore, the most significant weight, using the Logistic Function, was assigned to the regions with a distance to lineament <500 m following the Naghibi et al. [101] study (Figure 4g).

#### 4.1.8. Distance from Rivers

The distance from rivers plays a vital role in groundwater movement, water recharge, and hydrogeological systems [22]. Groundwater flows from the river to the groundwater zone increasing groundwater potential [107]. Thus, increasing the distance from the river leads to a decrease in groundwater recharge. According to the logistic transformation, the highest weight has been assigned to a distance of fewer than 220 m in this study area map [101](Figure 4h).

#### 4.2. Selecting Factors Influencing GWPA

The GWPA map is edited by integrating eight factors: permeability, slope, altitude, distances from lineaments and rivers, density of lineaments, drainage, and nodes. These factors were evaluated by both the normalized density ( $N_d$ ) and its weight ( $W_e$ ). The C-A fractal model (Figure 5a–h) was applied to determine thresholds for discretizing factor values to obtain classified maps (Figure 6a–h). Based on these maps, the P-A graphs were edited (Figure 7a–h).

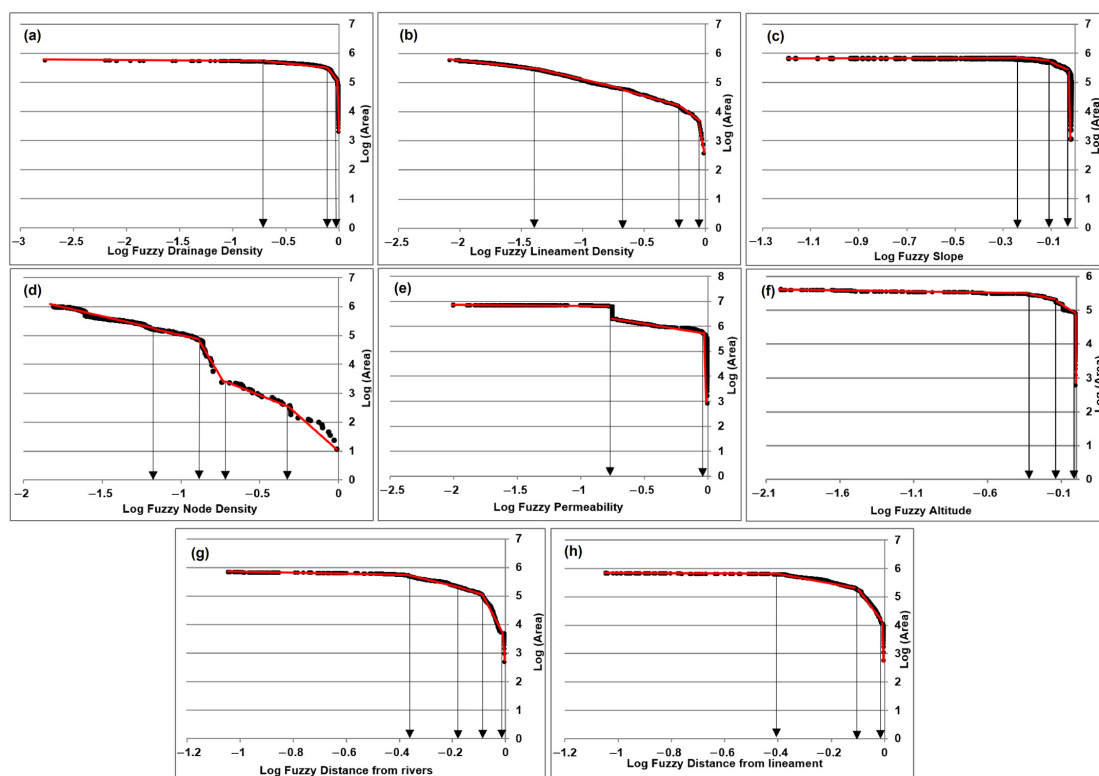


**Figure 5.** Concentration-area (C-A) log-log plots for the transformed values: (a) drainage density map; (b) lineament density map; (c) slope map; (d) node density map; (e) permeability map; (f) altitude map; (g) distance from rivers map; (h) distance from lineament map.



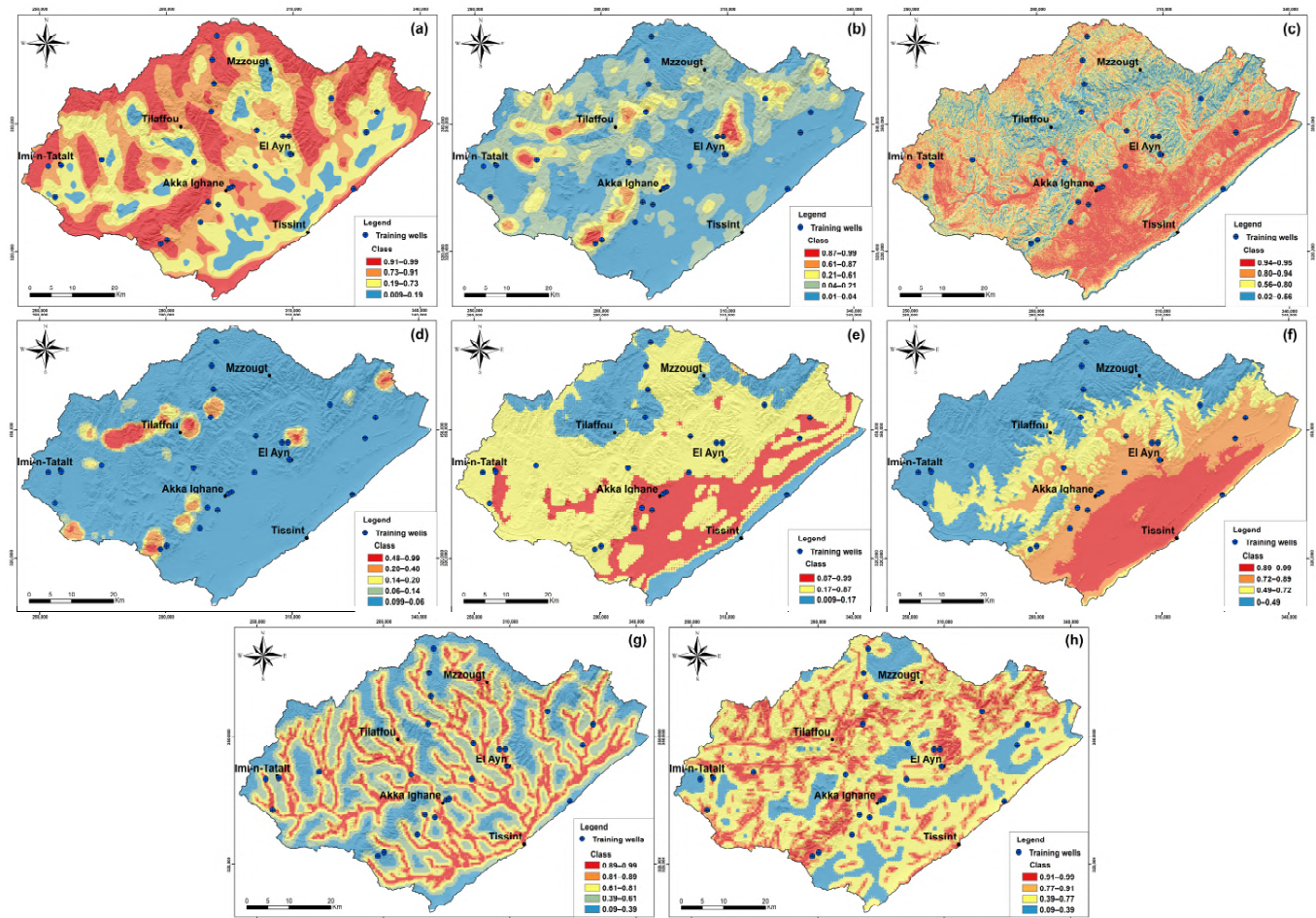


**Figure 6.** Classified map for the transformed values: (a) drainage density map; (b) lineament density map; (c) slope map; (d) node density map; (e) permeability map; (f) altitude map; (g) distance from rivers map; (h) distance from lineament map.

According to their importance based on P-A graph analysis (Table 2), we can show that (1) permeability and altitude with weights of 0.36 are the most important; (2) slope with a weight of 0.28 is the second criteria; (3) the distance from lineament and the distance from rivers with respectively 0.24 and 0.16, are the third criteria; followed by (4) lineament density and node density with 0.08 and 0.04. Finally, the drainage density was eliminated since it represents the value of  $N_d < 1$  and  $W_e < 0$ .

**Table 2.** The extracted parameters from the intersection point of P-A plots.

Evidential Map	Prediction Rate ( $P_r$ ) (%)	Occupied Area ( $O_a$ ) (%)	Normalized Density ( $N_d$ )	Weight ( $W_e$ )
Permeability	59	41	1.44	0.36
Altitude	59	41	1.44	0.36
Slope	57	43	1.33	0.28
Distance from lineament	56	44	1.27	0.24
Distance from rivers	54	46	1.17	0.16
Lineament density	52	48	1.08	0.08
Node density	51	49	1.04	0.04
Drainage density	45	55	0.82	−0.20

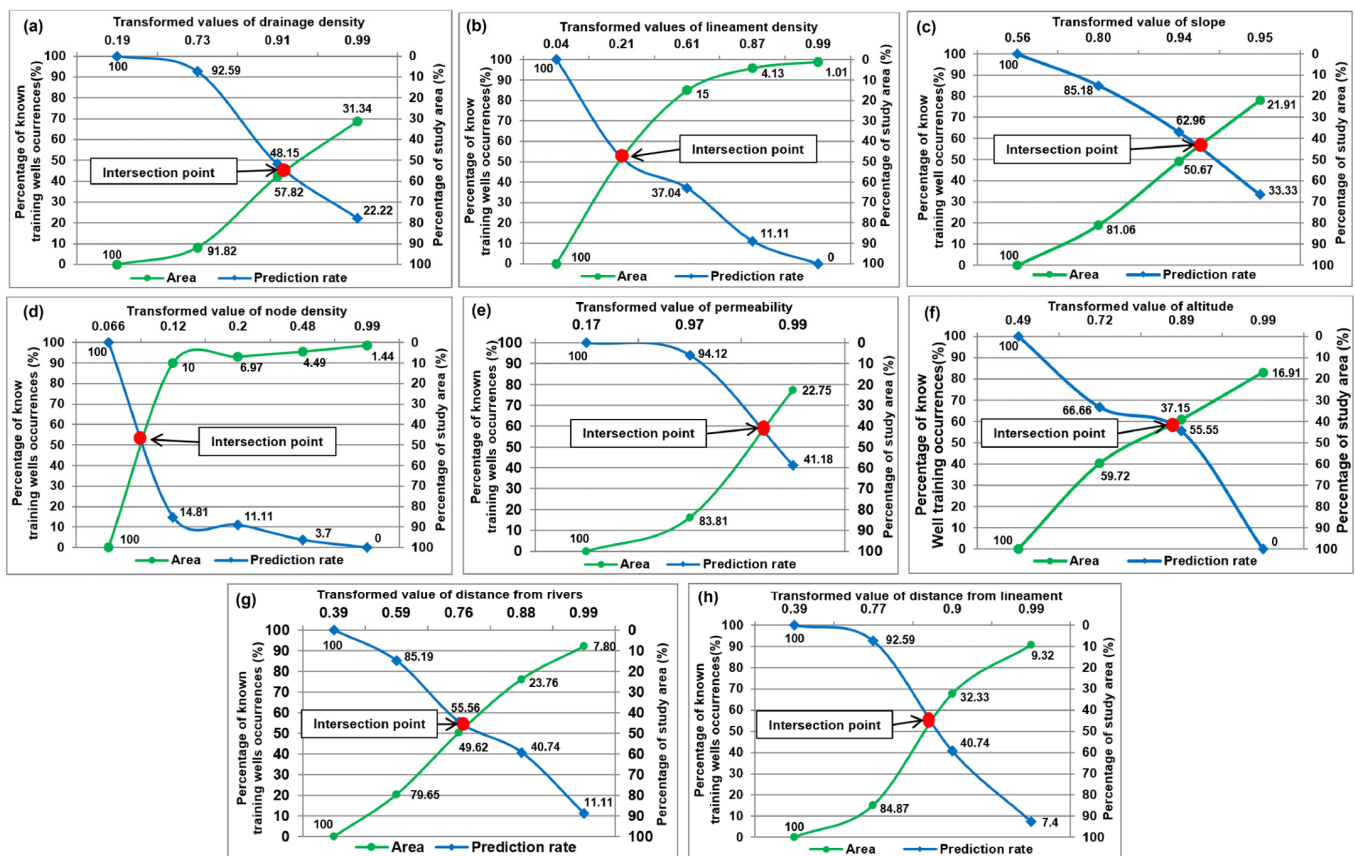


**Figure 7.** Prediction-area (P-A) plot for the classified map: (a) drainage density map; (b) lineament density map; (c) slope map; (d) node density map; (e) permeability map; (f) altitude map; (g) distance from rivers map; (h) distance from lineament map.

#### 4.3. Elaboration of Geometric Average Model

The Geometric Average is a method that can be applied as a multi-criteria decision-making approach to combine different factors [87]. It is applied only to transform values into a positive range using a logistic function before the integration [47]. However, we found that the geometric average yield has a better factor discriminating power [87]. According to Equation (6), the Geometric Average ( $G_{AGWPA}$ ) can be computed as:

$$G_{AGWPA}(F_{LD}, F_{SP}, F_{ND}, F_P, F_{AT}, F_{DFR}, F_{DFL}) = \left( \prod_{i=1}^7 F_i \right)^{1/7} = \sqrt[7]{F_{LD} F_{SP} F_{ND} F_P F_{AT} F_{DFR} F_{DFL}} \quad (6)$$

where  $G_{AGWPA}$  is the geometric average of groundwater potentiality,  $F_{LD}$ ,  $F_{SP}$ ,  $F_{ND}$ ,  $F_P$ ,  $F_{AT}$ ,  $F_{DFR}$ , and  $F_{DFL}$  are fuzzy scores of the lineament density, slope, node density, permeability, altitude, distance from rivers, and distance from lineament, computed using the logistic function. After the computation of  $G_{AGWPA}$  values of the Tissint basin, a geometric average potentiality model was generated (Figure 8a).

#### 4.4. Evaluation of Geometric Average Model

After elaborating on the potentiality map, the location of 26 known training well was used as test points in the P-A curve plot to assess the results [47]. For that, the C-A model (Figure 8b) was used to determine the threshold values for the classification of the geometric average values [20,67] (Figure 8a). Based on Figure 8b, the geometric average model was classified (Figure 8c), then the P-A plot (Figure 8d) was created as a model. The results show that  $N_d = 1.70$  ( $>1$ ) and  $W_e = 0.53$  ( $>0$ ). The geometric average model (Figure 8a) shows that 37% of the Tissint basin is a high-potential area, in which 63% of known training well are delineated, which illustrates the effectiveness of this model.

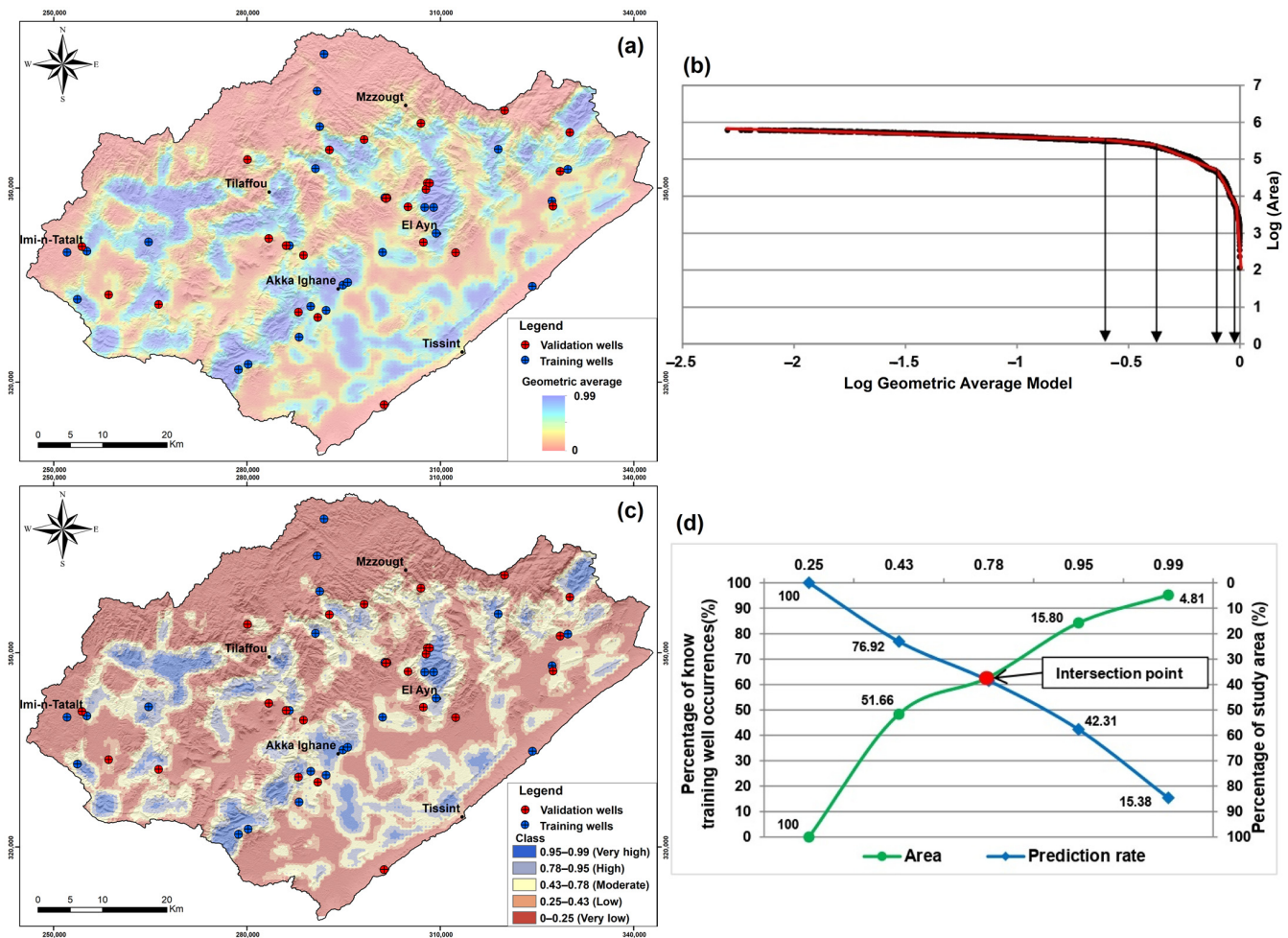


**Figure 8.** (a) Groundwater potentiality map of Tissint basin using the geometric average model; (b) Concentration-area (C-A) log-log plots of  $G_A$  GWPA; (c) Classified map of  $G_A$  GWPA; (d) Prediction-area (P-A) plot for the classed map of  $G_A$  GWPA.

#### 4.5. Validation of the Geometric Average Model

The GWPA map was validated by superimposing it on the 26 existing wells to confirm the result of the  $G_A$  GWPA model (Figure 8c, Table 3). The respective numbers of wells corresponding to very high, high, moderate, low, and very low groundwater potential areas are 1, 6, 5, 5, and 9. This result suggests a positive correlation between the wells location and the  $G_A$  GWPA model, especially in Akka Ighane, El Ayn, and Imi-n-Talat regions.

**Table 3.** The distribution of wells and percentage of areas in potential groundwater zones generated by the  $G_A$  GWPA model.

Class	Geometric Average Model ( $G_A$ GWPA)			
	Area (km <sup>2</sup> )	Area %	Number of Wells	Wells %
Very high	172.76	4.82	1	3.85
High	395.07	10.99	6	23.08
Moderate	767.77	21.36	5	19.23
Low	521.12	14.49	5	19.23
Very low	1737.56	48.34	9	34.61

## 5. Discussion

The  $G_A$  GWPA map edit was classified into five categories (Figure 8c): very high, high, moderate, low, and very low. Its analysis shows that the areas of high and very high



potentiality are related to the formation permeability factor, especially in the regions of El Ayn in the north, Akka Ighane in the southeast, Tilaffou in the west, and downstream of the basin. Arnous et al. [93] showed a strong relationship between high permeability formations and areas with high groundwater potentiality since it facilitates rain and wadi water infiltration. Deleting this factor at the mapping model level reduces the high and moderate potential regions alarmingly [104].

This permeability factor depends on lithological formations and becomes influential when lineaments fracture them. It is known that faults behave as conduits or barriers for groundwater flow depending on their kinematics and fault rock lithology [108,109]. In general, the interconnection of multiple fractures allows for water infiltration over large areas [110–112]. This fracture-permeability appears dominant in the basin's central and northwestern parts. The potentiality of such zones depends on the distances separating them from the recharge zones materialized in our case by the surface drainage network and its alluvial fill [16,113]. This recharge depends on the surface water circulation velocity depending on elevation and slope variations [6]. In the upstream part of the basin, the  $G_{A\text{ GWPA}}$  map shows low groundwater reserves due to steep slopes preventing water's gradual infiltration into deep reservoirs. On the other hand, porous alluvial formations characterize the downstream part of the basin with low gradients and longer water-formation contact time. The interconnection of these several factors led to the recharge of deep reservoirs and, thus, high groundwater potentiality. According to Ajay Kumar et al. [114], excluding the influence of slope in the mapping models has led to a significant increase in areas of low groundwater potentiality. Apart from these high potential areas, the rest of the basin is characterized by low geological formations permeability, high elevations inducing steep slopes, and low density of lineaments. These negatively impact water availability in these areas.

The effectiveness of  $G_{A\text{ GWPA}}$  in delineating potential groundwater areas shows an  $N_d$  greater than 1 and  $W_e$  greater than 0. However, all the factors used present prediction rates ( $P_r$ ) less ( $45 < P_r < 59$ ) than the geometric average model ( $P_r = 63$ ) (Figure 8d). Therefore, the target areas developed by these methods present positive associations with the existing wells. The validation results showed that approximately 46.16% of the well corresponds to areas of moderate to very high groundwater potentiality.

The  $G_{A\text{ GWPA}}$  map, although validated by existing wells, may have limitations due to the resolution of the data used in a study area. The application of satellite images and a high-resolution digital elevation model (DEM) allows better extraction of the factors influencing  $G_{A\text{ GWPA}}$  [16,61,115,116]. Consequently, the high resolution of these data improves the final  $G_{A\text{ GWPA}}$  map. The lack of a climatological station limits the integration of the precipitation factor. Therefore, it is important to equip the basin with a set of stations to fill this data gap.

## 6. Conclusions

Developing a reliable groundwater potential map requires advanced geology, hydrogeology, and satellite science. In addition, several factors interact to promote the recharge of deeper aquifers. Integrating these different factors into the Geometric Average model allowed the mapping of potential groundwater areas (GWPA) in the Tissint basin. Seven factors were considered in this model that allowed the development of the  $G_{A\text{ GWPA}}$  map, which was classified into five classes: very high, high, moderate, low, and very low, covering 4.82%, 10.99%, 21.36%, 14.49%, and 48.34% of the basin area. The P-A graph validated the  $G_{A\text{ GWPA}}$ .

The formation permeability factor presents the most significant impact among the others, although it is directly related to most of them. The areas located in the central and downstream part of the basin are characterized by a high water potentiality due to increased geological formations permeability near the drainage system, which constitutes a recharge zone, and a low slope allowing a prolonged water-formation contact time favoring a gradual infiltration of the water towards the deep aquifers.

The evaluation of the model results shows values of  $N_d = 1.70$  and  $W_e = 0.53$ , confirming the model's validity. The model results were compared with the 26 existing wells; 46.16% of them corresponded to areas of moderate to very high potential regions. These results confirm the suitability of the Geometric Average model for mapping potential groundwater zones. It can easily be applied in other similar areas to optimize future well locations.

**Author Contributions:** Conceptualization, F.Z.E. and S.B.; methodology, F.Z.E. and M.I.; software, F.Z.E.; validation, F.Z.E., S.B. and M.I.; formal analysis, F.Z.E. and M.I.; investigation, F.Z.E.; resources, F.Z.E.; data curation, F.Z.E.; writing—original draft preparation, F.Z.E., S.B., M.I., M.E.M., S.E. and H.E.A.; writing—review and editing, M.A. (Mohamed Abioui), M.A. (Mohamed Aadraoui), A.B., R.B.K., K.A. and M.S.F.; visualization, M.A. (Mohamed Abioui); supervision, S.B. and M.A. (Mohamed Abioui); project administration, M.A. (Mohamed Abioui); funding acquisition, K.A. All authors have read and agreed to the published version of the manuscript.

**Funding:** This research was funded by Researchers Supporting Project number (RSP2023R351), King Saud University, Riyadh, Saudi Arabia.

**Data Availability Statement:** Not applicable.

**Conflicts of Interest:** The authors declare no conflict of interest.

## References

- Margat, J.; van der Gun, J. *Groundwater around the World*; CRC Press/Balkema: Leiden, Netherlands, 2013.
- Smith, M.; Cross, K.; Paden, M.; Laban, P. *Spring—Managing Groundwater Sustainability*; IUCN: Gland, Switzerland, 2016.
- Kostyuchenko, Y.; Artemenko, I.; Abioui, M.; Benssaou, M. Global and Regional Climatic Modeling. In *Encyclopedia of Mathematical Geosciences*; Sagar, B.D., Cheng, Q., McKinley, J., Agterberg, F., Eds.; Springer: Cham, Switzerland, 2022; pp. 1–5. [\[CrossRef\]](#)
- Todd, D.K.; Mays, L.W. *Groundwater Hydrology*; Wiley: New York, NY, USA, 2005.
- Rekha, V.B.; Thomas, A.P. *Integrated Remote Sensing and GIS for Groundwater Potentially Mapping in Koduvu Ar-Sub-Watershed of Meenachil River Basin, Kottayam District*; School of Environmental Sciences, Mahatma Gandhi University: Kerala, India, 2007.
- Ozdemir, A. GIS-based groundwater spring potential mapping in the Sultan Mountains (Konya, Turkey) using frequency ratio, weights of evidence and logistic regression methods and their comparison. *J. Hydrol.* **2011**, *411*, 290–308. [\[CrossRef\]](#)
- Fankhauser, K.; Macharia, D.; Coyle, J.; Kathuni, S.; McNally, A.; Slinski, K.; Thomas, E. Estimating groundwater use and demand in arid Kenya through assimilation of satellite data and in-situ sensors with machine learning toward drought early action. *Sci. Total. Environ.* **2022**, *831*, 154453. [\[CrossRef\]](#)
- Aissa, R.B.; Boutoutaou, D. Characterization of groundwater in arid zones (case of Ouargla basin). *Energy Procedia* **2017**, *119*, 556–564. [\[CrossRef\]](#)
- Hssaisoune, M.; Bouchaou, L.; Sifeddine, A.; Bouimetarhan, I.; Chehbouni, A. Moroccan Groundwater Resources and Evolution with Global Climate Changes. *Geosciences* **2020**, *10*, 81. [\[CrossRef\]](#)
- Golkarian, A.; Rahmati, O. Use of a maximum entropy model to identify the key factors that influence groundwater availability on the Gonabad Plain, Iran. *Environ. Earth Sci.* **2018**, *77*, 369. [\[CrossRef\]](#)
- Naghibi, S.A.; Ahmadi, K.; Daneshi, A. Application of Support Vector Machine, Random Forest, and Genetic Algorithm Optimized Random Forest Models in Groundwater Potential Mapping. *Water Resour. Manag.* **2017**, *31*, 2761–2775. [\[CrossRef\]](#)
- Naghibi, S.A.; Pourghasemi, H.R.; Pourtaghi, Z.S.; Rezaei, A. Groundwater qanat potential mapping using frequency ratio and Shannon's entropy models in the Moghan watershed, Iran. *Earth Sci. Inform.* **2015**, *8*, 171–186. [\[CrossRef\]](#)
- Rahmati, O.; Naghibi, S.A.; Shahabi, H.; Bui, D.T.; Pradhan, B.; Azareh, A.; Rafiei-Sardooi, E.; Samani, A.N.; Melesse, A.M. Groundwater spring potential modelling: Comparing the capability and robustness of three different modeling approaches. *J. Hydrol.* **2018**, *565*, 248–261. [\[CrossRef\]](#)
- Aouragh, M.H.; Essahlaoui, A.; El Ouali, A.; El Hmaidi, A.; Kamel, S. Groundwater potential of Middle Atlas plateaus, Morocco, using fuzzy logic approach, GIS and remote sensing. *Geomat. Nat. Hazards Risk* **2017**, *8*, 194–206. [\[CrossRef\]](#)
- Hamdani, N.; Baali, A. Characterization of groundwater potential zones using analytic hierarchy process and integrated geomatic techniques in Central Middle Atlas (Morocco). *Appl. Geomat.* **2020**, *12*, 323–335. [\[CrossRef\]](#)
- Echogdali, F.Z.; Boutaleb, S.; Bendarma, A.; Saidi, M.E.; Aadraoui, M.; Abioui, M.; Ouchchen, M.; Abdelrahman, K.; Fnais, M.S.; Sajinkumar, K.S. Application of Analytical Hierarchy Process and Geophysical Method for Groundwater Potential Mapping in the Tata Basin, Morocco. *Water* **2022**, *14*, 2393. [\[CrossRef\]](#)
- Echogdali, F.Z.; Boutaleb, S.; Kpan, R.B.; Ouchchen, M.; Bendarma, A.; El Ayady, H.; Abdelrahman, K.; Fnais, M.S.; Sajinkumar, K.S.; Abioui, M. Application of Fuzzy Logic and Fractal Modeling Approach for Groundwater Potential Mapping in Semi-Arid Akka Basin, Southeast Morocco. *Sustainability* **2022**, *14*, 10205. [\[CrossRef\]](#)
- Souissi, D.; Msaddek, M.H.; Zouhri, L.; Chenini, I.; El May, M.; Dlala, M. Mapping groundwater recharge potential zones in arid region using GIS and Landsat approaches, southeast Tunisia. *Hydrol. Sci. J.* **2018**, *63*, 251–268. [\[CrossRef\]](#)

19. Mallick, J.; Khan, R.A.; Ahmed, M.; Alqadhi, S.D.; Alsubih, M.; Falqi, I.; Hasan, M.A. Modeling Groundwater Potential Zone in a Semi-Arid Region of Aseer Using Fuzzy-AHP and Geoinformation Techniques. *Water* **2019**, *11*, 2656. [\[CrossRef\]](#)
20. Machiwal, D.; Jha, M.K.; Mal, B.C. Assessment of Groundwater Potential in a Semi-Arid Region of India Using Remote Sensing, GIS and MCDM Techniques. *Water Resour. Manag.* **2010**, *25*, 1359–1386. [\[CrossRef\]](#)
21. Castillo, J.L.U.; Cruz, D.A.M.; Leal, J.A.R.; Vargas, J.T.; Tapia, S.A.R.; Celestino, A.E.M. Delineation of Groundwater Potential Zones (GWPZs) in a Semi-Arid Basin through Remote Sensing, GIS, and AHP Approaches. *Water* **2022**, *14*, 2138. [\[CrossRef\]](#)
22. Rahmati, O.; Pourghasemi, H.R.; Melesse, A.M. Application of GIS-based data driven random forest and maximum entropy models for groundwater potential mapping: A case study at Mehran Region, Iran. *Catena* **2016**, *137*, 360–372. [\[CrossRef\]](#)
23. Naghibi, S.A.; Vafakhah, M.; Hashemi, H.; Pradhan, B.; Alavi, S.J. Groundwater Augmentation through the Site Selection of Floodwater Spreading Using a Data Mining Approach (Case study: Mashhad Plain, Iran). *Water* **2018**, *10*, 1405. [\[CrossRef\]](#)
24. Rahmati, O.; Melesse, A.M. Application of Dempster–Shafer theory, spatial analysis and remote sensing for groundwater potentiality and nitrate pollution analysis in the semi-arid region of Khuzestan, Iran. *Sci. Total. Environ.* **2016**, *568*, 1110–1123. [\[CrossRef\]](#)
25. Haghizadeh, A.; Moghaddam, D.D.; Pourghasemi, H.R. GIS-based bivariate statistical techniques for groundwater potential analysis (an example of Iran). *J. Earth Syst. Sci.* **2017**, *126*, 109. [\[CrossRef\]](#)
26. Kordestani, M.D.; Naghibi, S.A.; Hashemi, H.; Ahmadi, K.; Kalantar, B.; Pradhan, B. Groundwater potential mapping using a novel data-mining ensemble model. *Hydrogeol. J.* **2019**, *27*, 211–224. [\[CrossRef\]](#)
27. Pourghasemi, H.R.; Beheshtirad, M. Assessment of a data-driven evidential belief function model and GIS for groundwater potential mapping in the Koohrang Watershed, Iran. *Geocarto Int.* **2014**, *30*, 662–685. [\[CrossRef\]](#)
28. Oh, H.-J.; Kim, Y.-S.; Choi, J.-K.; Park, E.; Lee, S. GIS mapping of regional probabilistic groundwater potential in the area of Pohang City, Korea. *J. Hydrol.* **2011**, *399*, 158–172. [\[CrossRef\]](#)
29. Moghaddam, D.D.; Rezaei, M.; Pourghasemi, H.R.; Pourtaghie, Z.S.; Pradhan, B. Groundwater spring potential mapping using bivariate statistical model and GIS in the Taleghan Watershed, Iran. *Arab. J. Geosci.* **2015**, *8*, 913–929. [\[CrossRef\]](#)
30. Ozdemir, A. Using a binary logistic regression method and GIS for evaluating and mapping the groundwater spring potential in the Sultan Mountains (Aksehir, Turkey). *J. Hydrol.* **2011**, *405*, 123–136. [\[CrossRef\]](#)
31. Chen, W.; Li, H.; Hou, E.; Wang, S.; Wang, G.; Panahi, M.; Li, T.; Peng, T.; Guo, C.; Niu, C.; et al. GIS-based groundwater potential analysis using novel ensemble weights-of-evidence with logistic regression and functional tree models. *Sci. Total. Environ.* **2018**, *634*, 853–867. [\[CrossRef\]](#) [\[PubMed\]](#)
32. Razandi, Y.; Pourghasemi, H.R.; Neisani, N.S.; Rahmati, O. Application of analytical hierarchy process, frequency ratio, and certainty factor models for groundwater potential mapping using GIS. *Earth Sci. Inform.* **2015**, *8*, 867–883. [\[CrossRef\]](#)
33. Hou, E.; Wang, J.; Chen, W. A comparative study on groundwater spring potential analysis based on statistical index, index of entropy and certainty factors models. *Geocarto Int.* **2018**, *33*, 754–769. [\[CrossRef\]](#)
34. Corsini, A.; Cervi, F.; Ronchetti, F. Weight of evidence and artificial neural networks for potential groundwater spring mapping: An application to the Mt. Modino area (Northern Apennines, Italy). *Geomorphology* **2009**, *111*, 79–87. [\[CrossRef\]](#)
35. Al Abadi, A.M.A.; Shahid, S. A comparison between index of entropy and catastrophe theory methods for mapping groundwater potential in an arid region. *Environ. Monit. Assess.* **2015**, *187*, 1–21. [\[CrossRef\]](#)
36. Rahmati, O.; Samani, A.N.; Mahdavi, M.; Pourghasemi, H.R.; Zeinivand, H. Groundwater potential mapping at Kurdistan region of Iran using analytic hierarchy process and GIS. *Arab. J. Geosci.* **2014**, *8*, 7059–7071. [\[CrossRef\]](#)
37. Yin, H.; Shi, Y.; Niu, H.; Xie, D.; Wei, J.; Lefticariu, L.; Xu, S. A GIS-based model of potential groundwater yield zonation for a sandstone aquifer in the Juye Coalfield, Shangdong, China. *J. Hydrol.* **2017**, *557*, 434–447. [\[CrossRef\]](#)
38. Moghaddam, D.D.; Rahmati, O.; Haghizadeh, A.; Kalantari, Z. A Modeling Comparison of Groundwater Potential Mapping in a Mountain Bedrock Aquifer: QUEST, GARP, and RF Models. *Water* **2020**, *12*, 679. [\[CrossRef\]](#)
39. Pham, B.T.; Son, L.H.; Hoang, T.-A.; Nguyen, D.-M.; Bui, D.T. Prediction of shear strength of soft soil using machine learning methods. *Catena* **2018**, *166*, 181–191. [\[CrossRef\]](#)
40. Tien Bui, D.; Shahabi, H.; Shirzadi, A.; Chapi, K.; Hoang, N.-D.; Pham, B.T.; Bui, Q.-T.; Tran, C.-T.; Panahi, M.; Bin Ahmad, B.; et al. A Novel Integrated Approach of Relevance Vector Machine Optimized by Imperialist Competitive Algorithm for Spatial Modeling of Shallow Landslides. *Remote Sens.* **2018**, *10*, 1538. [\[CrossRef\]](#)
41. Smith, A.J.; Walker, G.; Turner, J. Aquifer sustainability factor: A review of previous estimates. In *International Association of Hydrogeologists (IAH) and the Geological Society of Australia (GSA)*; CSIRO: Canberra, Australia, 2010; p. EP104589.
42. Naghibi, S.A.; Pourghasemi, H.R. A Comparative Assessment Between Three Machine Learning Models and Their Performance Comparison by Bivariate and Multivariate Statistical Methods in Groundwater Potential Mapping. *Water Resour. Manag.* **2015**, *29*, 5217–5236. [\[CrossRef\]](#)
43. Zabihi, M.; Pourghasemi, H.R.; Pourtaghi, Z.S.; Behzadfar, M. GIS-based multivariate adaptive regression spline and random forest models for groundwater potential mapping in Iran. *Environ. Earth Sci.* **2016**, *75*, 1–19. [\[CrossRef\]](#)
44. Chen, W.; Zhao, X.; Tsangaratos, P.; Shahabi, H.; Ilia, I.; Xue, W.; Wang, X.; Bin Ahmad, B. Evaluating the usage of tree-based ensemble methods in groundwater spring potential mapping. *J. Hydrol.* **2020**, *583*, 124602. [\[CrossRef\]](#)
45. Lee, S.; Hong, S.-M.; Jung, H.-S. GIS-based groundwater potential mapping using artificial neural network and support vector machine models: The case of Boryeong city in Korea. *Geocarto Int.* **2018**, *33*, 847–861. [\[CrossRef\]](#)



46. Naghibi, S.A.; Moghaddam, D.D.; Kalantar, B.; Pradhan, B.; Kisi, O. A comparative assessment of GIS-based data mining models and a novel ensemble model in groundwater well potential mapping. *J. Hydrol.* **2017**, *548*, 471–483. [\[CrossRef\]](#)
47. Yousefi, M.; Carranza, E.J.M. Geometric average of spatial evidence data layers: A GIS-based multi-criteria decision-making approach to mineral prospectivity mapping. *Comput. Geosci.* **2015**, *83*, 72–79. [\[CrossRef\]](#)
48. Yousefi, M.; Nykänen, V. Data-driven logistic-based weighting of geochemical and geological evidence layers in mineral prospectivity mapping. *J. Geochem. Explor.* **2016**, *164*, 94–106. [\[CrossRef\]](#)
49. Echogdali, F.Z.; Boutaleb, S.; Abia, E.H.; Ouchchen, M.; Dadi, B.; Id-Belqas, M.; Abioui, M.; Pham, L.T.; Abu-Alam, T.; Mickus, K.L. Mineral prospectivity mapping: A potential technique for sustainable mineral exploration and mining activities—A case study using the copper deposits of the Tagmout basin, Morocco. *Geocarto Int.* **2021**, 1–22. [\[CrossRef\]](#)
50. Afzal, P.; Mirzaei, M.; Yousefi, M.; Adib, A.; Khalajmasoumi, M.; Zarifi, A.Z.; Foster, P.; Yasrebi, A.B. Delineation of geochemical anomalies based on stream sediment data utilizing fractal modeling and staged factor analysis. *J. Afr. Earth Sci.* **2016**, *119*, 139–149. [\[CrossRef\]](#)
51. Choubert, G. Histoire géologique du précambrien de l'Anti-Atlas. *Notes Mem. Serv. Geol. Maroc.* **1963**, *162*, 352.
52. Soulaïmani, A.; Burkhard, M. The Anti-Atlas chain (Morocco): The southern margin of the Variscan belt along the edge of the West African craton. *Geol. Soc. Lond. Spec. Publ.* **2008**, *297*, 433–452. [\[CrossRef\]](#)
53. Benssaou, M.; Hamoumi, N. The western Anti-Atlas of Morocco: Sedimentological and palaeogeographical formation studies in the Early Cambrian. *J. Afr. Earth Sci.* **2001**, *32*, 351–372. [\[CrossRef\]](#)
54. Benssaou, M.; Hamoumi, N. Le graben de l'Anti-Atlas occidental (Maroc): Contrôle tectonique de la paléogéographie et des séquences au Cambrien inférieur. *C. R. Geosci.* **2003**, *335*, 297–305. [\[CrossRef\]](#)
55. Echogdali, F.Z.; Boutaleb, S.; Jauregui, J.; Elmouden, A. Cartography of Flooding Hazard in Semi-Arid Climate: The Case of Tata Valley (South-East of Morocco). *J. Geogr. Nat. Disasters* **2018**, *8*, 1–11. [\[CrossRef\]](#)
56. Ouchchen, M.; Boutaleb, S.; Abia, E.H.; El Azzab, D.; Abioui, M.; Mickus, K.L.; Miftah, A.; Echogdali, F.Z.; Dadi, B. Structural interpretation of the Igherm region (Western Anti Atlas, Morocco) from an aeromagnetic analysis: Implications for copper exploration. *J. Afr. Earth Sci.* **2021**, *176*, 104140. [\[CrossRef\]](#)
57. Echogdali, F.Z.; Boutaleb, S.; Taia, S.; Ouchchen, M.; Id-Belqas, M.; Kpan, R.B.; Abioui, M.; Aswathi, J.; Sajinkumar, K.S. Assessment of soil erosion risk in a semi-arid climate watershed using SWAT model: Case of Tata basin, South-East of Morocco. *Appl. Water Sci.* **2022**, *12*, 1–15. [\[CrossRef\]](#)
58. Choubert, G. L'accident majeur de l'Anti-Atlas. *C. R. Acad. Sci. Paris* **1947**, *224*, 1172–1173.
59. Thomas, R.; Chevallier, L.; Gresse, P.; Harmer, R.; Eglington, B.; Armstrong, R.; de Beer, C.; Martini, J.; de Kock, G.; Macey, P.; et al. Precambrian evolution of the Sirwa Window, Anti-Atlas Orogen, Morocco. *Precambrian Res.* **2002**, *118*, 1–57. [\[CrossRef\]](#)
60. Pham, B.T.; Jaafari, A.; Prakash, I.; Singh, S.K.; Quoc, N.K.; Bui, D.T. Hybrid computational intelligence models for groundwater potential mapping. *Catena* **2019**, *182*, 104101. [\[CrossRef\]](#)
61. Benjmel, K.; Amraoui, F.; Boutaleb, S.; Ouchchen, M.; Tahiri, A.; Touab, A. Mapping of Groundwater Potential Zones in Crystalline Terrain Using Remote Sensing, GIS Techniques, and Multicriteria Data Analysis (Case of the Ighrem Region, Western Anti-Atlas, Morocco). *Water* **2020**, *12*, 471. [\[CrossRef\]](#)
62. Bhattacharya, S.; Das, S.; Das, S.; Kalashetty, M.; Warghat, S.R. An integrated approach for mapping groundwater potential applying geospatial and MIF techniques in the semiarid region. *Environ. Dev. Sustain.* **2020**, *23*, 495–510. [\[CrossRef\]](#)
63. Micheli-Tzanakou, E. *Supervised and Unsupervised Pattern Recognition*; CRC Press: Boca Raton, FL, USA, 1999.
64. Berthold, M.; Hand, D.J. *Intelligent Data Analysis: An Introduction*; Springer: Berlin, Germany, 2003.
65. Bishop, C.M. *Pattern Recognition and Machine Learning*; Weller: New York, NY, USA, 2006.
66. Yousefi, M.; Kamkar-Rouhani, A.; Carranza, E.J.M. Application of staged factor analysis and logistic function to create a fuzzy stream sediment geochemical evidence layer for mineral prospectivity mapping. *Geochem. Explor. Environ. Anal.* **2014**, *14*, 45–58. [\[CrossRef\]](#)
67. Yousefi, M.; Carranza, E.J.M. Prediction–area (P–A) plot and C–A fractal analysis to classify and evaluate evidential maps for mineral prospectivity modeling. *Comput. Geosci.* **2015**, *79*, 69–81. [\[CrossRef\]](#)
68. Porwal, A.; Carranza, E.J.M.; Hale, M. A Hybrid Neuro-Fuzzy Model for Mineral Potential Mapping. *J. Int. Assoc. Math. Geol.* **2004**, *36*, 803–826. [\[CrossRef\]](#)
69. Porwal, A.; Carranza, E.J.M.; Hale, M. A Hybrid Fuzzy Weights-of-Evidence Model for Mineral Potential Mapping. *Nat. Resour. Res.* **2006**, *15*, 1–14. [\[CrossRef\]](#)
70. Mihalasky, M.J.; Bonham-Carter, G.F. Lithodiversity and Its Spatial Association with Metallic Mineral Sites, Great Basin of Nevada. *Nat. Resour. Res.* **2001**, *10*, 209–226. [\[CrossRef\]](#)
71. Daya, A.A. Comparative study of C–A, C–P, and N–S fractal methods for separating geochemical anomalies from background: A case study of Kamoshgaran region, northwest of Iran. *J. Geochem. Explor.* **2015**, *150*, 52–63. [\[CrossRef\]](#)
72. Heidari, S.M.; Afzal, P.; Ghaderi, M.; Sadeghi, B. Detection of mineralization stages using zonality and multifractal modeling based on geological and geochemical data in the Au–(Cu) intrusion-related Gouzal-Bolagh deposit, NW Iran. *Ore Geol. Rev.* **2021**, *139*, 104561. [\[CrossRef\]](#)
73. Afzal, P.; Alghalandis, Y.F.; Khakzad, A.; Moarefvand, P.; Omran, N.R. Delineation of mineralization zones in porphyry Cu deposits by fractal concentration–volume modeling. *J. Geochem. Explor.* **2011**, *108*, 220–232. [\[CrossRef\]](#)
74. Mandelbrot, B.B. *The Fractal Geometry of Nature*; Freeman: San Francisco, CA, USA, 1983.

75. Zissimos, A.M.; Cohen, D.R.; Christoforou, I.C.; Sadeghi, B.; Rutherford, N.F. Controls on soil geochemistry fractal characteristics in Lemesos (Limassol), Cyprus. *J. Geochem. Explor.* **2021**, *220*, 106682. [\[CrossRef\]](#)
76. Li, C.; Ma, T.; Shi, J. Application of a fractal method relating concentrations and distances for separation of geochemical anomalies from background. *J. Geochem. Explor.* **2003**, *77*, 167–175. [\[CrossRef\]](#)
77. Zuo, R.; Cheng, Q. Mapping singularities—A technique to identify potential Cu mineral deposits using sediment geochemical data, an example for Tibet, west China. *Miner. Mag.* **2008**, *72*, 531–534. [\[CrossRef\]](#)
78. Zuo, R. Decomposing of mixed pattern of arsenic using fractal model in Gangdese belt, Tibet, China. *Appl. Geochem.* **2011**, *26*, S271–S273. [\[CrossRef\]](#)
79. Cheng, Q.; Agterberg, F.; Ballantyne, S. The separation of geochemical anomalies from background by fractal methods. *J. Geochem. Explor.* **1994**, *51*, 109–130. [\[CrossRef\]](#)
80. Asl, R.A.; Afzal, P.; Adib, A.; Yasrebi, A.B. Application of multifractal modeling for the identification of alteration zones and major faults based on ETM+ multispectral data. *Arab. J. Geosci.* **2015**, *8*, 2997–3006. [\[CrossRef\]](#)
81. A Gonçalves, M.; Mateus, A.; Oliveira, V. Geochemical anomaly separation by multifractal modelling. *J. Geochem. Explor.* **2001**, *72*, 91–114. [\[CrossRef\]](#)
82. Cheng, Q.; Li, Q. A fractal concentration–area method for assigning a color palette for image representation. *Comput. Geosci.* **2002**, *28*, 567–575. [\[CrossRef\]](#)
83. Yousefi, M.; Carranza, E.J.M. Fuzzification of continuous-value spatial evidence for mineral prospectivity mapping. *Comput. Geosci.* **2015**, *74*, 97–109. [\[CrossRef\]](#)
84. Zuo, R.; Wang, J. Arc Fractal: An ArcGIS Add-In for Processing Geoscience Data Using Fractal/Multifractal Models. *Nat. Resour. Res.* **2020**, *29*, 3–12. [\[CrossRef\]](#)
85. Nazarpour, A.; Omran, N.R.; Paydar, G.R.; Sadeghi, B.; Matroud, F.; Nejad, A.M. Application of classical statistics, log ratio transformation and multifractal approaches to delineate geochemical anomalies in the Zarshuran gold district, NW Iran. *Geochemistry* **2015**, *75*, 117–132. [\[CrossRef\]](#)
86. Ouchchen, M.; Boutaleb, S.; Abia, E.; El Azzab, D.; Miftah, A.; Dadi, B.; Echogdali, F.; Mamouch, Y.; Pradhan, B.; Santosh, M.; et al. Exploration targeting of copper deposits using staged factor analysis, geochemical mineralization prospectivity index, and fractal model (Western Anti-Atlas, Morocco). *Ore Geol. Rev.* **2022**, *143*, 104762. [\[CrossRef\]](#)
87. Wang, Y.M.; Chin, K.-S.; Yang, J.B. Measuring the performances of decision-making units using geometric average efficiency. *J. Oper. Res. Soc.* **2007**, *58*, 929–937. [\[CrossRef\]](#)
88. Wei, G. Some Arithmetic Aggregation Operators with Intuitionistic Trapezoidal Fuzzy Numbers and Their Application to Group Decision Making. *J. Comput.* **2010**, *5*, 345–351. [\[CrossRef\]](#)
89. Tothill, P. Limitations of the use of the geometric mean to obtain depth independence in scanning and whole body counting. *Phys. Med. Biol.* **1974**, *19*, 382–385. [\[CrossRef\]](#)
90. Chung, C.-J.F.; Fabbri, A.G. Validation of Spatial Prediction Models for Landslide Hazard Mapping. *Nat. Hazards* **2003**, *30*, 451–472. [\[CrossRef\]](#)
91. Magesh, N.S.; Chandrasekar, N.; Soundranayagam, J.P. Delineation of groundwater potential zones in Theni district, Tamil Nadu, using remote sensing, GIS and MIF techniques. *Geosci. Front.* **2012**, *3*, 189–196. [\[CrossRef\]](#)
92. Arnous, M.O.; Sultan, Y.M. Geospatial technology and structural analysis for geological mapping and tectonic evolution of Feiran–Solaf metamorphic complex, South Sinai, Egypt. *Arab. J. Geosci.* **2014**, *7*, 3023–3049. [\[CrossRef\]](#)
93. Arnous, M.O. Groundwater potentiality mapping of hard-rock terrain in arid regions using geospatial modelling: Example from Wadi Feiran basin, South Sinai, Egypt. *Hydrogeol. J.* **2016**, *24*, 1375–1392. [\[CrossRef\]](#)
94. Jasrotia, A.S.; Bhagat, B.D.; Kumar, A.; Kumar, R. Remote Sensing and GIS Approach for Delineation of Groundwater Potential and Groundwater Quality Zones of Western Doon Valley, Uttarakhand, India. *J. Indian Soc. Remote. Sens.* **2013**, *41*, 365–377. [\[CrossRef\]](#)
95. Haris, K.; Efstratiadis, S.; Maglaveras, N.; Katsaggelos, A. Hybrid image segmentation using watersheds and fast region merging. *IEEE Trans. Image Process.* **1998**, *7*, 1684–1699. [\[CrossRef\]](#)
96. Boutaleb, S.; Boualoul, M.; Oudra, M.; Bouchaou, L.; Dindane, K. Apports du traitement d’image et de la géophysique à l’étude des ressources en eau en milieu fissuré: Cas de l’Anti-Atlas marocain. *Afr. Geosci. Rev.* **2008**, *15*, 129–141.
97. Boutaleb, S.; Boualoul, M.; Bouchaou, L.; Oudra, M. Application of remote-sensing and surface geophysics for groundwater prospecting in a hard rock terrain, Morocco. In *Applied Groundwater Studies in Africa*; CRC Press: London, UK, 2008; pp. 215–230. [\[CrossRef\]](#)
98. Boutaleb, S.; El Hammichi, F.; Tabyaoui, H.; Bouchaou, L.; Dindane, K. Détermination des écoulements préférentiels en zone karstique (Tafrata, Maroc), Apport des données satellitaires SAR ERS-1 et Landsat ETM+ et de la prospection géophysique. *Rev. Sci. Eau* **2009**, *22*, 407–419. [\[CrossRef\]](#)
99. Hssaisoune, M.; Boutaleb, S.; Bouchaou, L.; Benssaou, M.; Tagma, T. Use of remote sensing and electrical resistivity tomography to determine Tidsi spring recharge and underground drainage. *Eur. Water* **2017**, *57*, 429–434.
100. Rahman, M.A.; Rusteberg, B.; Gogu, R.; Ferreira, J.L.; Sauter, M. A new spatial multi-criteria decision support tool for site selection for implementation of managed aquifer recharge. *J. Environ. Manag.* **2012**, *99*, 61–75. [\[CrossRef\]](#)

101. Naghibi, S.A.; Pourghasemi, H.R.; Dixon, B. GIS-based groundwater potential mapping using boosted regression tree, classification and regression tree, and random forest machine learning models in Iran. *Environ. Monit. Assess.* **2016**, *188*, 1–27. [\[CrossRef\]](#)
102. Acharya, T. Study of Groundwater Prospects of the Crystalline Rocks in Purulia District, West Bengal, India Using Remote Sensing Data. *Earth Resour.* **2013**, *1*, 54. [\[CrossRef\]](#)
103. Saranya, T.; Saravanan, S. Groundwater potential zone mapping using analytical hierarchy process (AHP) and GIS for Kancheepuram District, Tamilnadu, India. *Model. Earth Syst. Environ.* **2020**, *6*, 1105–1122. [\[CrossRef\]](#)
104. Patra, S.; Mishra, P.; Mahapatra, S.C. Delineation of groundwater potential zone for sustainable development: A case study from Ganga Alluvial Plain covering Hooghly district of India using remote sensing, geographic information system and analytic hierarchy process. *J. Clean. Prod.* **2018**, *172*, 2485–2502. [\[CrossRef\]](#)
105. Ganapuram, S.; Kumar, G.V.; Krishna, I.M.; Kahya, E.; Demirel, M.C. Mapping of groundwater potential zones in the Musi basin using remote sensing data and GIS. *Adv. Eng. Softw.* **2009**, *40*, 506–518. [\[CrossRef\]](#)
106. Solomon, S.; Quiel, F. Groundwater study using remote sensing and geographic information systems (GIS) in the central highlands of Eritrea. *Hydrogeol. J.* **2006**, *14*, 1029–1041. [\[CrossRef\]](#)
107. Aswathi, J.; Sajinkumar, K.S.; Rajaneesh, A.; Oommen, T.; Bouali, E.H.; Kumar, R.B.B.; Rani, V.R.; Thomas, J.; Thrivikramji, K.P.; Ajin, R.S.; et al. Furthering the precision of RUSLE soil erosion with PSInSAR data: An innovative model. *Geocarto Int.* **2022**, 1–24. [\[CrossRef\]](#)
108. Caine, J.S.; Evans, J.P.; Craig, B.F. Fault zone architecture and permeability structure. *Geology* **1996**, *24*, 1025–1028. [\[CrossRef\]](#)
109. Faulkner, D.; Jackson, C.; Lunn, R.; Schlische, R.; Shipton, Z.; Wibberley, C.; Withjack, M. A review of recent developments concerning the structure, mechanics and fluid flow properties of fault zones. *J. Struct. Geol.* **2010**, *32*, 1557–1575. [\[CrossRef\]](#)
110. Goldscheider, N.; Neukum, C. Fold and fault control on the drainage pattern of a double-karst-aquifer system, Winterstaude, Austrian Alps. *Acta Carsologica* **2010**, *39*, 173–186. [\[CrossRef\]](#)
111. Evans, J.P.; Forster, C.B.; Goddard, J.V. Permeability of fault-related rocks, and implications for hydraulic structure of fault zones. *J. Struct. Geol.* **1997**, *19*, 1393–1404. [\[CrossRef\]](#)
112. Medici, G.; Smeraglia, L.; Torabi, A.; Botter, C. Review of Modeling Approaches to Groundwater Flow in Deformed Carbonate Aquifers. *Groundwater* **2020**, *59*, 334–351. [\[CrossRef\]](#) [\[PubMed\]](#)
113. Jothibas, A.; Anbazhagan, S. Modeling groundwater probability index in Ponnaiyar River basin of South India using analytic hierarchy process. *Model. Earth Syst. Environ.* **2016**, *2*, 1–14. [\[CrossRef\]](#)
114. Kumar, V.A.; Mondal, N.C.; Ahmed, S. Identification of Groundwater Potential Zones Using RS, GIS and AHP Techniques: A Case Study in a Part of Deccan Volcanic Province (DVP), Maharashtra, India. *J. Indian Soc. Remote. Sens.* **2020**, *48*, 497–511. [\[CrossRef\]](#)
115. Mohammadzadeh, A.; Zoj, M.J.V.; Tavakoli, A. Automatic main road extraction from high resolution satellite imageries by means of particle swarm optimization applied to a fuzzy-based mean calculation approach. *J. Indian Soc. Remote. Sens.* **2009**, *37*, 173–184. [\[CrossRef\]](#)
116. Benjmel, K.; Amraoui, F.; Aydda, A.; Tahiri, A.; Yousif, M.; Pradhan, B.; Abdelrahman, K.; Fnais, M.S.; Abioui, M. A Multidisciplinary Approach for Groundwater Potential Mapping in a Fractured Semi-Arid Terrain (Kerdous Inlier, Western Anti-Atlas, Morocco). *Water* **2022**, *14*, 1553. [\[CrossRef\]](#)

**Disclaimer/Publisher’s Note:** The statements, opinions and data contained in all publications are solely those of the individual author(s) and contributor(s) and not of MDPI and/or the editor(s). MDPI and/or the editor(s) disclaim responsibility for any injury to people or property resulting from any ideas, methods, instructions or products referred to in the content.